



Soft Matter

**Design rules for glass formation from model molecules
designed by a neural-network-biased genetic algorithm**

Journal:	<i>Soft Matter</i>
Manuscript ID	SM-ART-07-2019-001486.R1
Article Type:	Paper
Date Submitted by the Author:	03-Sep-2019
Complete List of Authors:	Meenakshisundaram, Venkatesh; University of Akron, Department of Polymer Engineering Hung, Jui-Hsiang; University of Akron, Department of Polymer Engineering Simmons, David; University of South Florida, Department of Chemical and Biomedical Engineering

SCHOLARONE™
Manuscripts



Design rules for glass formation from model molecules designed by a neural-network-biased genetic algorithm

Venkatesh Meenakshisundaram,^a Jui-Hsiang Hung^a and David S. Simmons^{b*}

Received 00th January 20xx,
Accepted 00th January 20xx

DOI: 10.1039/x0xx00000x

www.rsc.org/

The glass transition – an apparent amorphous solidification process – is a central feature of the physical properties of soft materials such as polymers and colloids. A key element of this phenomenon is the observation of a broad spectrum of deviations from an Arrhenius temperature of dynamics in glass-forming liquids, with the extent of deviation quantified by the “fragility” of glass formation. The underlying origin of “fragile” glass formation and its dependence on molecular structure remain major open questions in condensed matter physics and soft materials science. Here we employ molecular dynamics simulations, together with a genetic algorithm, to design and study model rigid molecules spanning a broad range of fragilities of glass formation. Results indicate that fragility of glass formation can be controlled by tuning molecular asphericity, with extended molecules tending to exhibit low fragilities and compact molecules tending toward higher fragilities. The glass transition temperature itself, on the other hand, correlates well with high-temperature activation behavior and with density. These results point the way towards rational design of glass-forming liquids spanning a range of dynamical behavior, both via these physical insights and via future extensions of this evolutionary design strategy to real chemistries. Finally, we show that results compare well with predictions of the Nonlinear Langevin Theory of liquid dynamics, which is a precursor of the more recently developed Elastically Collective Nonlinear Langevin Equation Theory of Mirigian and Schweizer, identifying this framework as a promising basis for molecular design of the glass transition.

Introduction

The effort to understand the nature of the glass transition and its dependence on molecular properties is a grand challenge of soft materials science^{1–4}. The most distinctive feature of this transition is the deviation of the structural relaxation time, τ_α , from an Arrhenius temperature dependence upon cooling^{5–8}. The field presently lacks a generally accepted chemically predictive theory of this transition^{2,3}. It is thus generally not possible to predict at what temperature and by how much dynamics will deviate from the Arrhenius rate law for a particular molecular structure, making first-principles chemical prediction of the glass transition temperature T_g and associated dynamics presently intractable.

At the same time, the glass transition is of central importance to the properties and performance of many technological materials and liquids. The ability to predict and design this transition in an efficient manner would be of great value for applications ranging from structural materials to next generation batteries^{9–11} to biopreservative formulations^{12,13}. Control of both the glass transition temperature and of the temperature dependence of relaxation dynamics in its immediate vicinity would be of particular value.

Dynamics in the vicinity of the glass transition are commonly quantified by two figures of merit: the glass transition temperature itself, and the kinetic fragility index m , which is a measure of the T_g -normalized thermal ‘abruptness’ of the transition. The kinetic fragility index is specifically defined via the equation¹⁴

$$m = \left. \frac{d \log \tau}{dT_g/T} \right|_{T=T_g}, \quad (1)$$

where τ is the segmental relaxation time. The combination of T_g and m describes the temperature dependence of the relaxation time in the vicinity of T_g . Values of m range from ~ 16 for fluids obeying an Arrhenius rate law to values in excess of 200 for fluids exhibiting strong growth in the apparent activation energy of relaxation on cooling¹⁵.

Access to molecular structures yielding a broad range of fragilities is of both fundamental and practical interest. Fundamentally, exploration of the upper limit of fragilities (if one exists) would permit study of particularly abrupt glass transitions and might therefore provide insight into underlying length scales of mechanisms associated with the glass transition³. In addition, a considerable number of competing theoretical frameworks have been proposed to explain the glass transition^{2,3}; the question of how to determine which of these frameworks is correct is arguably the central challenge of the field. Since non-Arrhenius dynamics are indisputably a central aspect of the glass-transition phenomenon, an ability to

^a Department of Polymer Engineering, University of Akron..

^b Department of Chemical and Biomedical Engineering, University of South Florida, Tampa, Florida 33612, USA. Email: dssimmons@usf.edu Electronic Supplementary Information (ESI) available. See DOI: 10.1039/x0xx00000x

describe glass-formation behaviour in liquids spanning a broad range of fragility must arguably be one central test of the viability of each of these frameworks. Development of simple model molecules spanning a wide range of fragilities would therefore be of considerable fundamental theoretical value.

From a practical standpoint, independent control of T_g and fragility would be of great value, as it would permit design of materials in which the temperature of apparent solidification and the temperature dependence of viscosity above this temperature could be rationally tuned to yield targeting processing behaviour, thermal response, and mechanical properties. Fragility itself has also been correlated (although not conclusively) with a number of material properties of direct relevance to material performance^{12,16,17}, such that discovery of particularly high or low fragility glasses could provide access to new engineering properties.

Here we employ molecular dynamics simulations to explore the relationship between coarse features of molecular shape and resulting glass formation behaviour. We first simulate a series of rigid trimers of variable central bond angle as a minimal model for the relationship between shape and glass formation behaviour. We then employ a neural-network-biased genetic algorithm¹⁸ to design, in simulation, model 4-bead and 6-bead rigid bodies exhibiting extremes (high and low) of fragility of glass formation. The results are employed to correlate the glass transition temperature and fragility with molecular shape and with thermodynamic properties of the system. We ultimately compare these findings with predictions^{19–22} of the Nonlinear Langevin Equation theory²³ of supercooled liquid dynamics.

Methodology

Molecular Dynamics Simulation Model

We employ molecular dynamics simulations to study the dynamics and glass formation of rigid model molecules comprised of Lennard Jones beads with fixed internal degrees of freedom. Model molecules are designed via a scheme similar to that of Miskin et al.²⁴ In this scheme, two beads are initially placed at their contact distance d in the middle of a generation box, with their centre-to-centre vector aligned on the z axis. The third bead is then dropped towards the centre of the box along a polar angle ϕ with respect to the z-axis and is stopped as soon as it contacts either of the initial beads at its contact distance d . A fourth bead is then dropped towards the centre from infinite distance along a line specified by a polar angle ϕ and azimuthal angle θ . Again, it is frozen in place as soon as it contacts any bead at distance d . This final step is then repeated as many times as necessary with additional beads to achieve the desired number n of total beads per molecule. Representative model molecules resulting from this scheme are illustrated in Figure 1.

Beads in distinct rigid molecules interact via a 12-6 Lennard-Jones (LJ) potential:

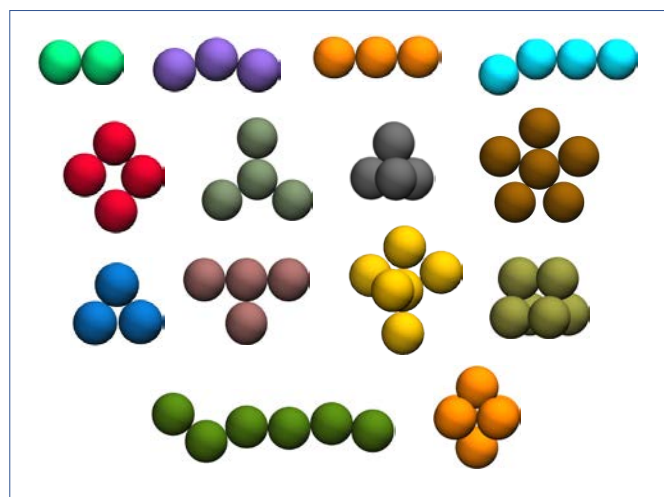


Figure 1. Example model molecule geometries probed in this study

$$E_{LJ}^{ij} = 4\epsilon_{ij} \left[\left(\frac{\sigma_{ij}}{r} \right)^{12} - \left(\frac{\sigma_{ij}}{r} \right)^6 \right] \quad (2)$$

where ϵ_{ij} sets the interaction energy scale, σ_{ij} sets the range of the interaction, and r is the distance between two beads in dimensionless LJ units.

Each simulated system includes many molecules of a single shared geometry. Recent work has indicated that monodisperse trimers are highly crystallization prone^{25–27}. In order to suppress crystallization, in each simulation two different scaled molecule sizes – A and B – are employed. These scaled sizes represent an extension of the Kob-Anderson²⁸ binary mixture parameters from the spherical-molecule fluid to structured molecules. Specifically, interaction length scales for interactions between beads in distinct A aggregates or distinct B aggregates are given by $\sigma_{AA} = 1.0$ and $\sigma_{BB} = 0.88$. The contact distance d within each rigid body is scaled with the self-interaction length scale, such that $d_i = \sigma_{ij}$. Interactions between beads in A and B aggregates have a scale given by $\sigma_{AB} = 0.8$. Similarly, interaction energy parameters are given by $\epsilon_{AA} = 1.0$, $\epsilon_{BB} = 0.5$, and $\epsilon_{AB} = 1.5$. For each pair of particles of types i and j , interactions are truncated at a distance $r_{ij,cut} = 2.5\sigma_{ij}$, such that interactions include the attractive tail of the potential. In any given simulation, 80% of molecules are of type A and 20% are of type B . Each simulation incorporates a total of 4800 beads. These parameters are equivalent to those employed in the binary LJ fluid, with the extension of rescaling the intramolecular contact distance with σ . At the level of spherical-particle fluids, this type of model has been widely employed to study supercooled fluids dynamics and glass formation, such that it makes an excellent basis for the study of glass formation in systems with more complex molecular structure^{4,29–31}.

Simulations are performed in the LAMMPS molecular dynamics simulation package³². Molecules are modelled as rigid via the “rigid” package³³ in LAMMPS. Simulations are performed at a constant pressure $P = 0$, using a Nose-Hoover thermostat and barostat with damping parameters of $2 \tau_U$ and $5 \tau_U$ for temperature and pressure control, respectively. Simulations

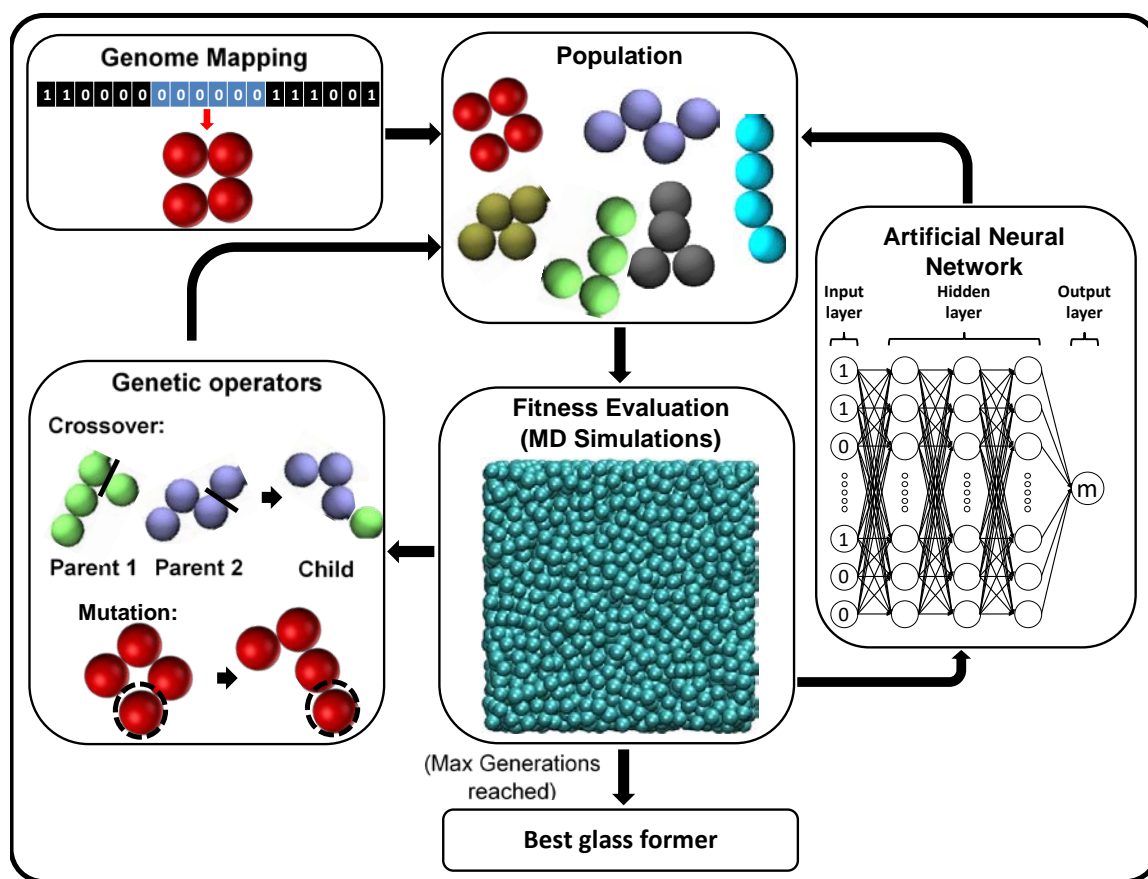


Figure 2: Schematic of NBGA for designing model glass formers

employ Verlet time integration³⁴ with a time step size of 0.01. In order to prevent any possible net momentum buildup over extremely long simulation times, the net linear and angular momentum of the simulation box is reset to zero every 10^6 timesteps.

We employ the Predictive Stepwise Quench (PreSQ) algorithm to efficiently simulate dynamics in these systems in an automated manner. Details of this algorithm can be found in our prior publication³⁵. In summary, this algorithm functions as follows. For each system, an initial random configuration is generated with the PACKMOL software package³⁶. This configuration is subject to an initial high temperature equilibration, followed by a thermal quench. Temperatures from this quench are selected for further equilibration via an algorithm that attempts to select temperatures yielding an approximately even spacing in relaxation time τ_α , using an extrapolation from higher temperature data to estimate relaxation times at successively lower temperatures. Configurations at each of these temperatures are then subject to an isothermal isobaric annealing period, for a timescale at least ten times the predicted τ_α at that temperature; this prediction is then automatically checked against the simulated relaxation time, and temperatures not actually satisfying the $10\tau_\alpha$ equilibration time requirement are discarded. This verification of equilibration for a period many times the structural relaxation time is a standard method of ensuring

equilibration in the simulation literature^{37–48}. After reaching equilibrium, data are then collected over an additional period of approximately ten times τ_α . In order to retain computational tractability given the large number of systems simulated here, we employ an upper limit relaxation time of $10^4 \tau_U$ (corresponding to a maximum annealing time of $10^5 \tau_U$) and report data only for temperatures with relaxation times equal to or less than this value.

Simulation Analysis

We quantify relaxation dynamics of these systems based on the reorientational autocorrelation function given by $C_2(t) = \langle P_2[e_i(0), e_i(t)] \rangle$, where P_2 is the second Legendre polynomial and e_i is the unit vector along a chosen intramolecular vector. Here we specifically employ the vector between the two most distant beads within a given rigid body. We then define τ_α as the time at which $C_2(t)$ decays to a value of 0.2, employing a fit to a Kohlrausch-Williams-Watts (KWW) stretched exponential function for data smoothing and interpolation. This approach is consistent with the use of this correlation function to determine structural relaxation times in other simulated systems^{49,50} and is closely related to dynamical information obtained via experimental dynamic light scattering techniques.

In order to obtain T_g and m from simulation, we first fit relaxation time data across a range of temperature to the Vogel-Fulcher-Tammann (VFT) equation^{51–53},

$$\tau_\alpha = \tau_0 \exp\left[\frac{DT_0}{T - T_0}\right], \quad (3)$$

where τ_0 is an extrapolated high-temperature relaxation time, T_0 is an extrapolated divergence temperature, and D is a breadth parameter. At this point, there are two philosophically distinct approaches possible to the determination of T_g and m . The first approach is to define these quantities on the timescale at which the simulations fall from equilibrium – in this case $10^4 \tau_L$. This approach yields values referred to as the *computational* dynamic glass transition temperature $T_{g,c}$ and fragility m_c . The second approach is to employ the VFT form to extrapolate to a timescale associated with experimental glass formation – approximately $10^{14} \tau_L$. This approach yields values referred to as the extrapolated experimental dynamic glass transition temperature $T_{g,e}$ and fragility m_e . In our view, the former approach is often preferable when extracting qualitative trends, since the lack of extrapolation yields results with less noise and extrapolation uncertainty. The latter approach is necessary, however, when one wishes to obtain values that are more directly comparable to experimentally observed ranges of T_g and m . In the design process described below, which relies upon correct rank-ordering of fragility, we therefore employ computational values. When discussing the physics of designed systems, we focus on extrapolated values as being more comparable to experiment, and values of T_g and m shown without subscripts in figures throughout the manuscript correspond to the extrapolated experimental-timescale quantity.

Neural-network-biased generic algorithm for design of model glass formers.

Model glass formers are designed using a neural-network-biased genetic algorithm (NBGA) described in our previous work^{18,54}. A schematic of the NBGA workflow is shown in Figure 2. The algorithm functions as follows.

We describe the structure of candidate molecules via a genetic mapping to a binary sequence. Each genetic sequence maps to a rigid molecule geometry by specifying the azimuthal (θ) and polar (ϕ) angles employed in generating the rigid body, as follows. Each angle is specified by a 6-bit sequence within the binary genome. A 6-bit genome provides 64 (2^6) unique combinations. The angular resolution is thus 5.625° . These angles are represented in a sequence within the genome: bits 1–6 represent the ϕ of the third bead, bits 7 through 12 and 13 through 18, respectively, represent the θ and ϕ for the fourth bead, and so on. For 3-bead glass formers, the shape of the molecule is represented by a 6-bit binary genome and for 6-bead glass formers, the shape of the molecule is represented by a 42-bit binary genome.

The NBGA begins with a random population of 32 molecular geometries. After this initial random population, the majority of

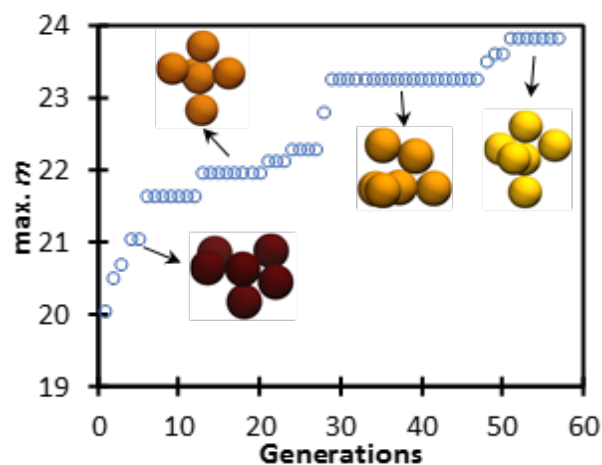


Figure 3. Sample improvement in computational-timescale fragilities accessed by the genetic algorithm over ~60 generations of the algorithm for a 6-bead model molecule, with graphics showing molecular shapes corresponding to various fragilities.

future candidates in the genetic algorithm are selected via the standard algorithm. Within this algorithm, the fitness of each candidate (i.e. the degree of match to the target properties) is assessed via molecular dynamics simulations. Each system is simulated in parallel as described in the previous section. The computational kinetic fragility index, m_c , is used as a raw fitness value when designing for high fragility. When designing for low fragility, the raw fitness value is defined as $100 - m$. The raw fitness is then linearly scaled to between 0 and 1 within each given generation in order to maintain constant selection pressure. Two distinct parents are chosen via fitness-proportionate roulette wheel selection. A ‘child’ candidate is then generated via two-point crossover. This generated child candidate is subject to a low point-mutation rate of 0.01 per bit. These genetic operations are repeated until two less than the quota of new candidates are filled. At the same time, the best candidate from the prior generation of the NBGA is passed directly to this new generation as well, without modification (an operation known as “elitism”). As in the case of our previous studies,^{18,54} if a previously simulated candidate is re-generated in the NBGA, the fitness value is obtained from a global census storing prior results, instead of simulating the system again, and the population size for that generation is then incremented by one. This maintains a constant number of new simulation-based fitness evaluations per generation, enabling efficient use of computational resources.

The neural network biasing employed to accelerate the genetic algorithm functions as follows. Once fitness evaluation is completed for a particular generation of glass formers, all data generated by the GA up to that point is sent to an artificial neural network (ANN). After each generation of the main genetic algorithm completes, the ANN is retrained employing all of the data accumulated to that point. Prior to beginning the next generation of the main genetic algorithm, a distinct genetic algorithm is run, using ANN predictions for fitness evaluation. Because ANN-based fitness evaluation is extremely fast, this ANN can search through hundreds of thousands of projected candidates in a time period much shorter than that needed for

a single generation of the main GA, and waiting for its completion does not appreciably delay the overall GA. This secondary genetic algorithm specifically seeks the candidate predicted to be best by this neural-network. This best projected candidate is then added as a 'suggestion' to the next generation of the NBGA. This suggestion is employed as the final candidate in the next generation of the main GA and is subject to the same simulation-based fitness evaluation as candidates obtained via genetic operators. If this projected candidate is poor, it typically does not survive the selection process and does not appreciably alter the design cycle. However, if the candidate is highly performing, its genes ultimately spread through the GA population and accelerate the design cycle.

Within this strategy, in the initial few generations of the NBGA, only limited data are available to train neural network. As the number of generations increase, the neural network actively re-trains itself every generation as data becomes available, making its predictions more effective. This increase in effectiveness enables faster convergence of the NBGA relative to standard genetic algorithms¹⁸. Prior validation work has indicated that this approach can yield considerably accelerated convergence relative to a classical genetic algorithm¹⁸.

Each system was simulated with 2 CPUs per temperature and required approximately 2.1 days of wall time. The entire process of the NBGA, including MD simulations, ANN, PreSQ, and analysis is fully automated and involves no human intervention.

Here we study 3-bead, 4-bead and 6-bead model glass formers. All possible shapes for 3-bead glass formers were studied since only 64 3-bead shapes (each corresponding to a different angle for the 3-bead body) are possible with the employed mapping scheme. 4-bead and 6-bead systems were designed with the NBGA for both high fragility glass forming shapes and low fragility (strong) glass forming shapes. For each number of beads, the NBGA was first employed to design for high fragility. As shown by Figure 3, this algorithm yields rapid increases in the computational-timescale fragility employed for fitness determination during fragility maximization. In an ensuing NBGA designing for low fragility, the entire data set of systems probed in that high fragility study was pre-loaded into the NBGA neural network. This prevents the re-simulation of a vast number of candidates and enables much faster convergence to strong glass forming shapes.

In addition to the systems above, we also attempted to perform a genetic design cycle employing 8-bead model glass-formers. However, the entire relaxation time temperature dependence for these systems shifts upward with increasing molecular size, such that it becomes increasingly difficult to access the supercooled liquid regime with increasing bead-number. With the simulation resources available, results indicated that it was not possible to obtain sufficient access to the glass-formation range in 8-bead molecules to permit reliable determination of T_g and m , and we thus exclude these systems from analysis of glass-formation dynamics.

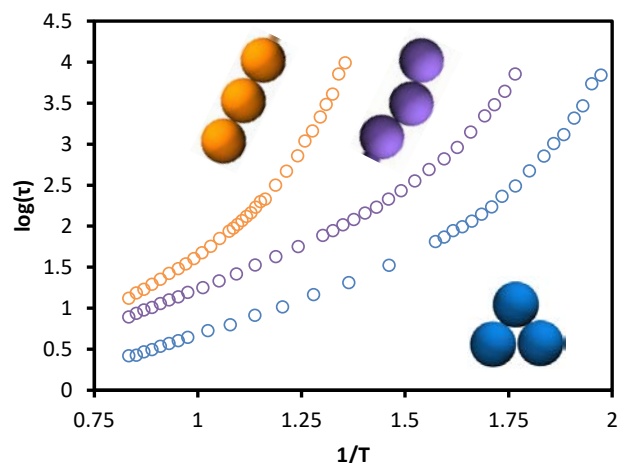


Figure 4. Arrhenius plot of relaxation times for several representative 3-bead model molecular glass formers.

Results

Trimers

We begin by considering the dynamics of the family of trimeric rigid bodies and their dependence on shape. A similar family of hard core, monodisperse hard spheres was recently simulated in two and three dimensions with a focus on jamming and crystallization behaviour^{25,26}; here we focus on dynamics and glass formation behaviour. Because the trimer contains only a single effective structural variable – the angle between beads 1, 2, and 3, we can simulate molecules spanning this entire space. As shown by Figure 4 for three representative geometries, the range of relaxation time temperature dependences that can be obtained simply by varying this angle is remarkably large. Indeed, at an inverse temperature of 1.25, this figure reveals a ~ 3 order of magnitude separation between the relaxation of a straight trimer and a closed 3-body ring, with this separation evidently growing dramatically on further cooling.

In order to better quantify these differences and their dependence on shape in this family of trimers, we consider the dependence of glass transition temperature T_g and kinetic fragility index m on the trimer central angle θ (we note that this quantity is not equivalent to the angles involved in the generation procedure of these multibodies, described above). Here we have employed an extrapolation via the VFT form to a timescale of 10^{14} τ_L , roughly comparable to experimental timescales, in obtaining m and T_g . However, we have additionally computed T_g and m at a timescale of 10^4 , which involves little extrapolation from these simulation data. This choice does not alter our qualitative findings.

As shown in Figure 5a, there are three notable features in the dependence of T_g and m of these trimers on angle. First, both T_g and m exhibit a minimum in the vicinity of 140° to 152° . The minimum of fragility at 152° corresponds to the purple molecules in Figure 4; it is essentially a slightly bent rod. Second, for trimers with angle greater than about 150° , increasing θ

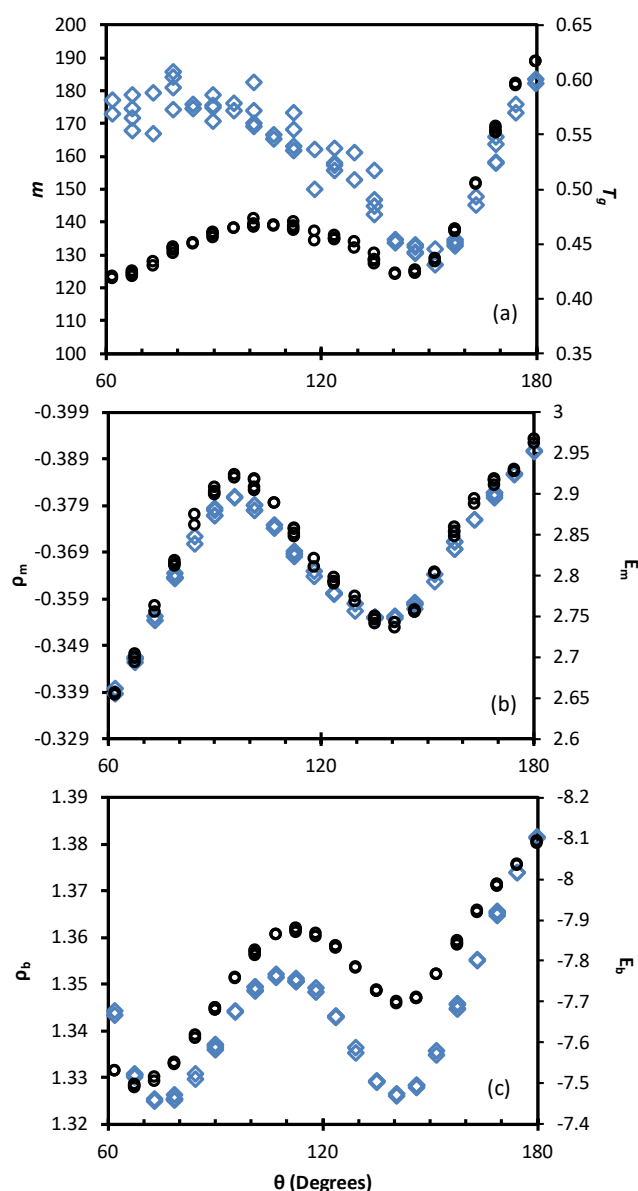


Figure 5. Plots, vs central trimer angle θ , of the following: (a) T_g (black circles) and m (blue diamonds); (b) temperate dependence parameters for pair energy (black circles) and density (blue diamonds); (c) 0 K extrapolated intercept parameters for pair energy (black circles) and density (blue diamonds). Plots include all trimers simulated.

dramatically increases T_g , with an accompanying increase in fragility. Remarkably, an alteration of only 30° , from 150° to 180° , leads to an approximate 50% increase in T_g . The slowest-relaxing trimer is therefore the rod (the orange molecule in Figure 4). Finally, there is a broad region for $\theta < 150^\circ$ in which T_g and m exhibit qualitatively different behaviour. Fragility progressively increases with approach to the three-membered ring. However, unlike for near-linear trimers, this increase in fragility is not accompanied by a comparable increase in T_g . Instead, T_g rises and passes through a weak maximum in the vicinity of $\theta = 106^\circ$ before dropping again to a value near its global minimum.

How can we understand these trends? We first ask whether they are connected to underlying thermodynamic variables

such as density and cohesive energy that are implicated in glass formation by a theoretical frameworks in which the glass transition is associated with underlying thermodynamic and packing phenomena^{8,55,56}. Fragility in particular has often been connected to the quality of molecular packing or to “packing frustration”, with the proposition that at fixed interactions better molecular packing tends to yield lower fragilities. For example, the Generalized Entropy Theory of glass formation⁸, which combines the Adam Gibbs theory for glass formation⁵⁶ with a Lattice Cluster theory for molecular structure and thermodynamics^{57,58}, predicts that less fragile molecules are those that “fill space better than stiffer molecules”. The meaning of the term “packing” outside of the context of lattice models is somewhat ill-defined. However, a reasonable interpretation is that, holding all interactions equal and within a chemically homogeneous series of species, we might expect a higher occupied volume fraction in less fragile glass formers.

The set of systems simulated here is chemically quite homogeneous, and since there is no variation in the per-bead volume between systems, we can employ the number density ρ of beads (not of molecules) as one reasonable measure of molecular packing. We specifically focus on the number density of beads within the simulation and on the average per-bead pair-energy. The complication is now that the quantities are naturally temperature dependent and these systems have distinct T_g 's, and so it is not entirely clear how to perform a comparison of ρ or cohesive energy among systems. However, both of these quantities generally exhibit an approximately linear temperature dependence above T_g . To quantify their trends with θ without the need to select a particular temperature of comparison, we therefore employ linear fits to these quantities and extract an extrapolated zero-temperature value of each, denoted ρ_b and E_b , and a strength of the temperature dependence of each, denoted ρ_m and E_m :

$$\rho \cong \rho_m T + \rho_b \quad (4)$$

and

$$E \cong E_m T + E_b \quad (5)$$

Both slope variables are closely related to a thermodynamic susceptibility. ρ_b is related to the constant pressure thermal expansion; E_b reflects a partial specific heat encoding only information about pairwise interaction energies.

As shown in Figure 5 b and c, the trend observed in T_g with varying θ is mirrored by trends in energy and density: both slopes and extrapolated low temperature limits of both values exhibit extrema in the vicinity of 100° and 140° . This qualitative correspondence is consistent with a scenario wherein shapes that pack more tightly exhibit higher densities and higher cohesive energies, even at fixed pairwise interaction strength. These trends can be expected to increase the activation barrier to relaxation, leading to higher T_g s.

We note that these results exhibit intriguing similarities with data recently published by Griffith and Hoy for simulations of the *jamming* behaviour of bent hard-core trimers²⁵. There, the

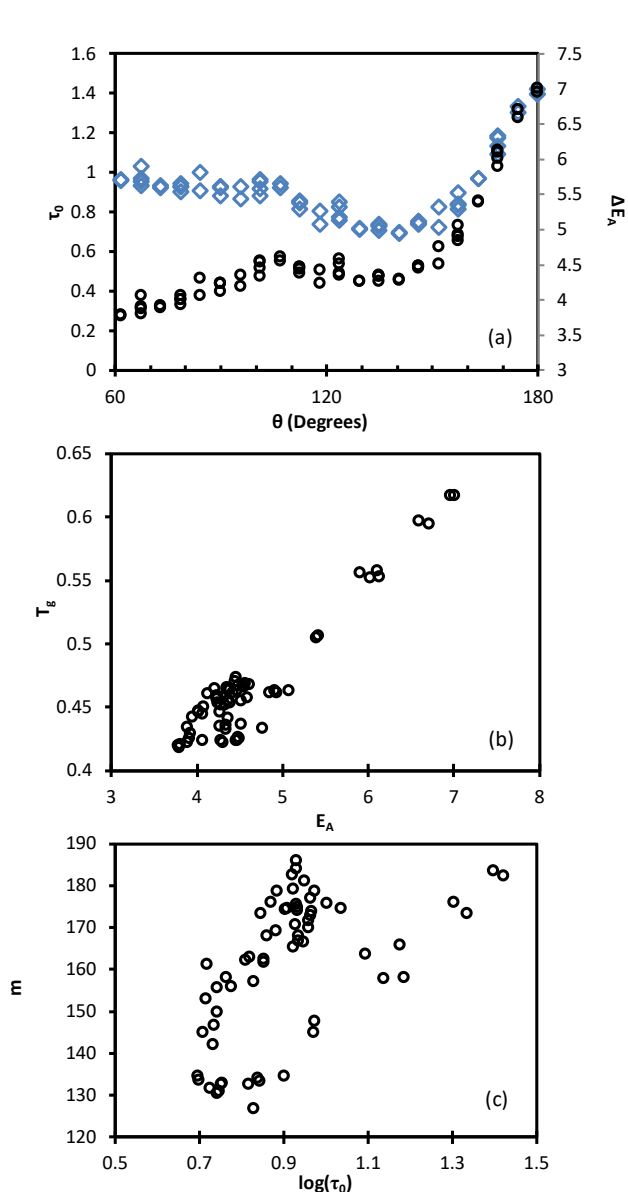


Figure 6. (a) Plot vs trimer central angle θ of high temperature activation barrier (black circles) and high-temperature Arrhenius pre-factor (blue diamonds). (b) Extrapolated T_g vs high-temperature Arrhenius activation barrier. (c) Extrapolated fragility vs high-temperature Arrhenius pre-factor. Plots include all trimers simulated.

jamming packing fraction was shown to exhibit a dependence on bond angle that strongly mirrors the T_g dependence on angle in Figure 5a: they found that linear trimers exhibited very low jamming volume fractions (corresponding to high T_g 's), highly bend trimers exhibited a very high jamming volume fraction (corresponding to low T_g 's), with a local maximum and minimum in between. The features qualitatively accord with those we find for T_g , suggesting a close connection between athermal jamming and thermal glass formation in this class of systems. We note that this is quite different from the θ dependence of the crystallization behaviour of both athermal and thermal trimers in both two and three dimensions, which exhibit maximal crystalline packings for both triangles and straight rods^{25–27}.

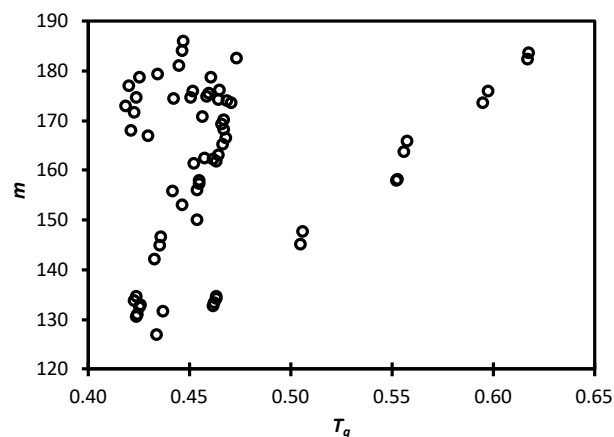


Figure 7. Fragility vs T_g for all trimers simulated.

To what extent do trends observed in Figure 5 emerge from shifts in dynamics at high temperature, above the range of temperatures directly associated with glass formation? The demarcation point between the “glass formation range” and the high-temperature activation range is often defined as the temperature T_A above which dynamics roughly obey an Arrhenius temperature dependence:

$$\tau \cong \tau_0 \exp\left(\frac{E_A}{kT}\right) \quad (6)$$

In order to probe the relationship between T_g , m and high-temperature activation behaviour in these 3-mers, we therefore perform a fit of relaxation times above T_A to equation (6) for each 3-mer simulated. As shown in Figure 6a, E_A behaves in a qualitatively similar manner to T_g , while $\log(\tau_0)$ behaves in a manner similar to m with varying θ . Figure 6b demonstrates that there is in fact an appreciable correlation between T_g and the high temperature activation barrier, although this correlation is dominated by the high- T_g wing of the data with $\theta > 150$ and essentially vanishes at lower θ . Figure 6c indicates that there may be some complex correlation between m and $\log(\tau_0)$ but that there is certainly no simple relationship between these quantities.

We thus observe a strong and rich dependence of relaxation dynamics on shape for rigid trimers, even at fixed site-site interaction strength. Notably, as emphasized by Figure 7, these model molecules do not exhibit a rough expected proportionality between T_g and fragility⁵⁹; instead, these quantities are not strongly correlated. While these model molecules cannot be literally mapped to a particular chemical structure, they are relevant to the understanding of the qualitative relationship between coarse molecular shape and glass formation behaviour in real molecules. These initial findings thus suggest the possibility of using molecular shape to rationally control fragility and T_g as independent variables, providing access to a broad array of targeted temperature-dependent relaxation behaviours.

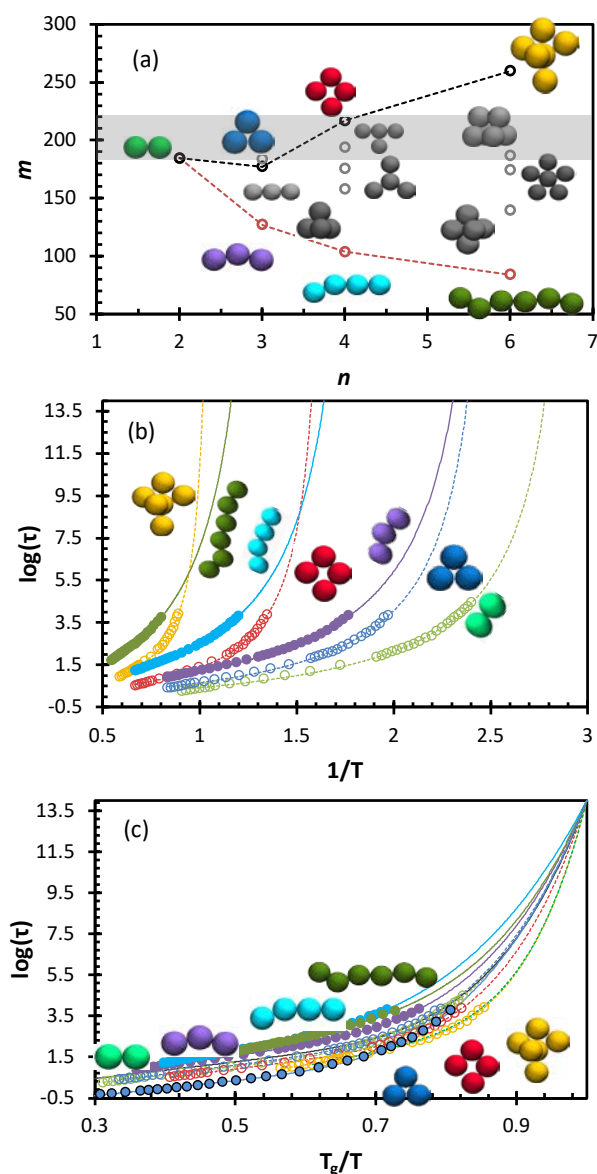


Figure 8. (a) Maximal (black circles) and minimal (red circles) fragilities discovered as a function of number of beads per molecule. Colored images show structures of maximal and minimal fragility molecules. Additional images and associated points show structures and fragilities of several human-design molecules with simple symmetries. (b) Arrhenius plots of relaxation time vs inverse temperature for the extremal molecules shown in part (a). (c) Same as (b), but with the x-axis normalized by the extrapolated T_g for each model species.

Behaviour of 4-mers and 6-mers from evolutionary design

The natural question now is to what degree these findings can be extended to larger and more complex model molecules. It is also of interest to explore whether more structurally complex molecules can provide access to a larger range of T_g s and fragilities than those achievable with trimers.

In Figure 8, we plot the maximal and minimal experimental-timescale fragilities discovered by the genetic algorithm for each molecular size. As can be seen there, the range of possible fragilities grows with increasing size of the model molecules. The grey bar in this figure indicates the range of fragilities commonly accessed via the standard Kremer-Grest bead-spring

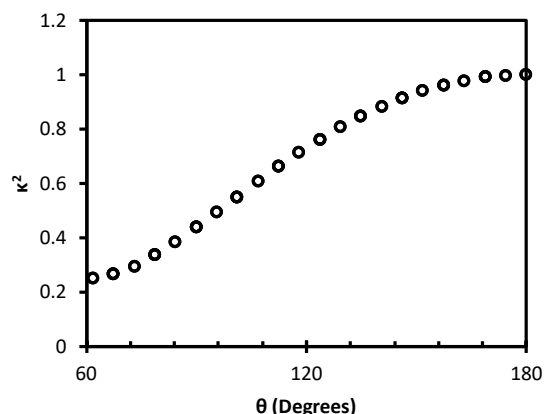


Figure 9. Plot of relative anisotropy index of trimers vs timer central angle.

polymer and the standard binary Lennard Jones model: approximately $m = 185$ to $m = 220$. By comparison, the $n = 6$ model molecules exhibit a fragility range of approximately 80 to 260 based upon the VFT extrapolation to experimental time scales. This large range is achieved purely via alterations in molecular shape, at fixed pairwise cohesive interaction. This naturally raises the question of how fragility depends on shape in these molecules and whether it mirrors the findings reported above for trimers.

Qualitatively, the 'extremal' molecular geometries shown in Figure 8 appear to be consistent with the findings in trimers: extremely low fragilities are associated with *nearly* extended shapes that contain at least one bend; high fragilities are associated with relatively compact shapes. In this case, however, we do not have a natural variable such as θ against which to parameterize this variation for the entire population of molecules studied. Inspired by the observation that the 'extendedness' of the molecule appears to play a key role for both 3-mers and for these large molecules, we employ the relative shape anisotropy κ^2 as a shape metric. κ^2 is computed for each molecule from the principle components of its gyration tensor as

$$\kappa^2 \equiv \frac{3}{2} \frac{\lambda_1^4 + \lambda_2^4 + \lambda_3^4}{(\lambda_1^2 + \lambda_2^2 + \lambda_3^2)^2} - \frac{1}{2} \quad (7)$$

where the λ_k^2 is the k^{th} principle component of the gyration tensor of the molecule. κ^2 is bounded from 0 to 1, with a value of 0 for a perfect sphere and a value of 1 for an infinite line. Increasing values of κ^2 thus denote increasing 'extendedness' of the molecule. As shown by Figure 9, for the trimers κ^2 maps to θ in a monotonic manner.

We also tested the use of the asphericity index and acylindricity index as shape metrics; these metrics give qualitatively similar results as κ^2 for individual molecular sizes. However, collapses across multiple molecule sizes were generally poorer, likely because these quantities are not bounded from 0 to 1 and are not well normalized for the size of the object.

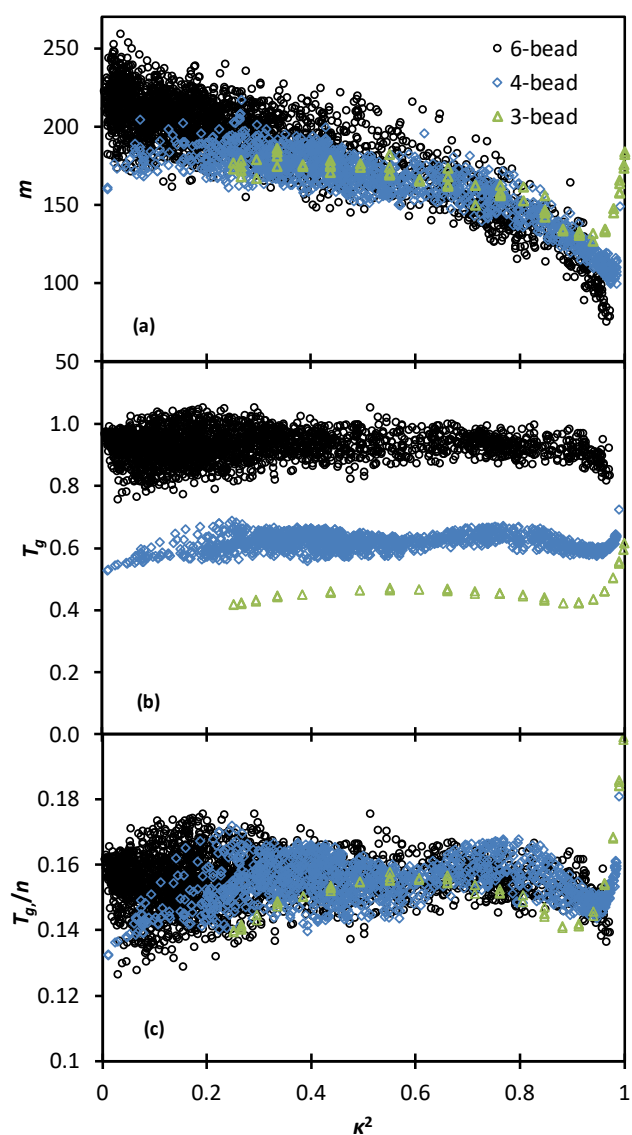


Figure 10. Plots vs relative anisotropy index of (a) fragility, (b) T_g , and (c) T_g/n , for all 3-bead (green triangles), 4-bead, (blue diamonds), and 6-bead (black circles) rigid molecules simulated by the genetic algorithm.

As shown in Figure 10a, increases in shape anisotropy generally tend to correlate with decreases in fragility. A linear fit to this relationship gives a coefficient of determination $R^2 = 0.77$ for the three data sets combined, indicating that more than three quarters of the variation in fragility can be predicted by variations in relative shape anisotropy (R^2 values for correlations on a per-molecule-size basis are reported in the SI, along with a table of R^2 values for many other correlations tested in this study). This trend is consistent with the observation from Figure 8a that the least fragile of the molecules are extended while the most fragile are compact.

A notable exception to this trend is the upturn in fragility for extremely linear 3-mers reported in the prior section. There is some evidence for an attenuated equivalent of this upturn in the 4-mers. This is most evident in a large increase in fragility for the 4-mer with highest κ^2 . Even excluding this point,

however, analysis of the data for glass formers with $0.95 < \kappa^2 < 1$ suggests an upturn for the most extended 4-mers: both a quadratic fit to this domain and a smoothing spline, excluding the single highest- κ^2 molecule, identify an upturn at the highest values of κ^2 . No such upturn is present in the 6-mers, for which the only observable trend is a strong tendency towards lower fragilities with increasing relative shape anisotropy.

There thus appear to be, in principle, two high-fragility shape regimes. First, highly compact shapes tend to yield high fragilities. Second, extremely linear shapes tend to exhibit high fragilities. There are potential implications of this latter regime for the glass formation behaviour of polymers. There, increases in chain stiffness are typically mapped to an increasingly large statistical segment length, which implies an increasingly extended underlying quasi-rigid element of the chain. Polymer fragility commonly increases with chain stiffness⁶, which within this picture would be a natural outcome of a more extended underlying dynamical unit in this near-linear regime. Outside of polymers (for which longer-range connectivity tends to frustrate rapid crystallization) we expect that access to this near-linear regime may frequently be prohibited by incipient liquid crystallization. Linear rigid rods have a strong tendency to form liquid crystals⁶⁰; simulations of thermal rods as short as length 5, for example, have been shown to exhibit a rich liquid crystalline phase diagram that would likely commonly prohibit access to glass-formation in this regime⁶¹.

We now turn to the question of the dependence of the glass transition temperature on molecular structure. It is evident in Figure 10b that T_g scales most predominantly with the molecule size rather than molecular anisotropy. Normalizing T_g by the number of beads n per molecule leads in Figure 10c to a reasonable collapse of T_g data for all of the molecule sizes probed. This finding is consistent with the proposition that the size of the relaxing unit is a fundamental determinant of structural relaxation times and T_g . Indeed, the Elastically Cooperative Nonlinear Langevin Equation theory of glass formation predicts that T_g should increase with the size of the relaxing unit (as measured by the number of “rigidly moving sites” within the relaxing dynamical unit), both where the relaxing unit is a single molecule and where it is a Kuhn segment within a polymer chain^{62–64}. Similarly, experimental data for a series of OTP analogues⁶⁵ are consistent with a scenario wherein T_g scales with molecular size at roughly fixed chemistry, as is the increase in T_g from glucose to trehalose (a glucose dimer)⁶⁶.

With this normalization by molecular size applied, we can now consider the issue of any dependence of T_g on molecular anisotropy. In the 4-mers, there is some evidence of a non-monotonic dependence of T_g on κ^2 in a manner similar to the trimers: a local minimum for nearly extended molecules (around $\kappa^2 = 0.94$); a sharp upturn for the most highly extended molecules; and a non-monotonic trend passing through a soft maximum with κ^2 decreasing below 0.94 (Figure 10c). For the 6-mer, these trends are largely lost. The high κ^2 upturn is missing, as is any apparent dependence of T_g on κ^2 beyond

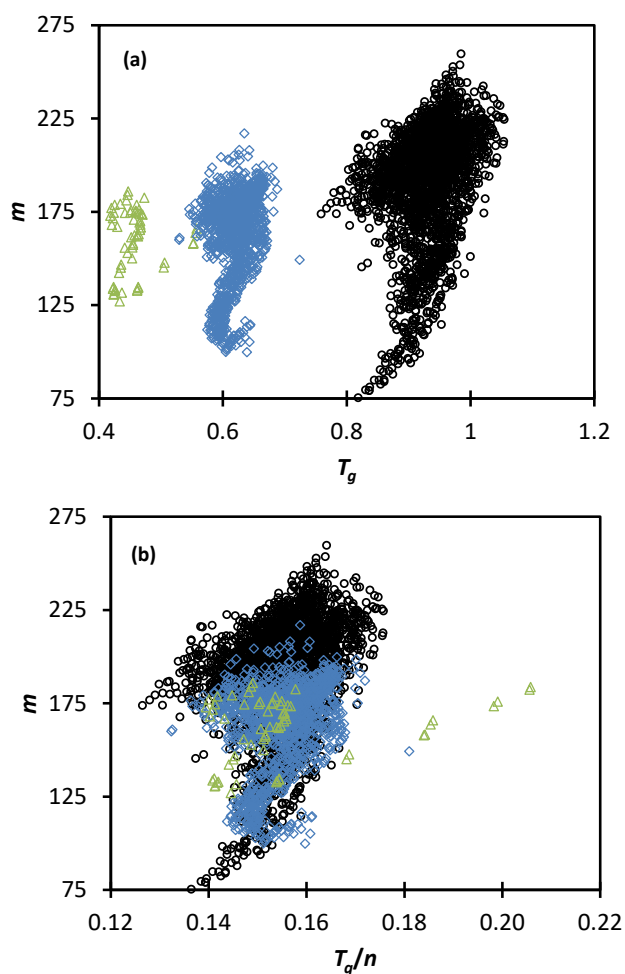


Figure 11. (a) Fragility vs T_g and (b) Fragility vs T_g/n , for all 3-bead (green triangles), 4-bead, (blue diamonds), and 6-bead (black circles) rigid molecules simulated by the genetic algorithm.

scatter for $\kappa^2 < 0.9$. The data do, however, retain a minimum in T_g around $\kappa^2 \cong 0.95$. Evidently, the finding that slightly bent rods tend to lie at a minimum of both T_g and fragility is a fairly robust one.

One important implication of the observation that T_g scales with molecule size while m does not is that there can evidently be no general correlation between these two quantities, even at fixed pairwise interaction strength. This can be seen in Figure 11a, where T_g is shown to increase with n while m remains roughly constant on average. However, even if we account for the molecular size effect on T_g (Figure 11b), no general correlation is observed between these two quantities. The single exception to this is in the limit of nearly linear molecules with $n = 3$ and $n = 4$, where increases in T_g correlate with increases in m . Although this limit corresponds to a very small fraction of the systems simulated here, it may be quite relevant to understanding the glass formation behaviour of semi-flexible polymers. These polymers commonly possess Kuhn segments – expected to approximately correspond to the fundamental unit – on the order of 3-5 chemical repeat units long. As noted above, these Kuhn segments can be naturally quite extended,

since the chain is inflexible on length scales smaller than the Kuhn segment. Fragility fairly commonly scales roughly with T_g in these semiflexible polymers⁶, consistent with the proposition that they may commonly correspond to this ‘extended rigid body’ limit at the level of a Kuhn segment. Moreover, both T_g and fragility typically increase with chain stiffness in polymers⁶. Increasing chain stiffness is commonly mapped to an increasing number of chemical repeat units within a statistical segment of the chain, which would in turn map to a more extended near-rigid subunit of the chain – a situation consistent with the trend observed here at a monomeric level.

Interrelations between dynamic and thermodynamic quantities

It is now of evident interest to understand to understand why T_g and m are generally uncorrelated and what underlying factors and mechanisms control each quantity. We begin by again considering the dependence of T_g and m on the density and interaction energy of the system. As with the trimers, we face the complication that both of these quantities are temperature dependent, and we therefore employ fits to equations (4) and (5) to extract slope and intercept parameters characterizing these quantities.

Before probing the relationship between these thermodynamic quantities and relaxation dynamics, we first note the existence of a relationship between the slope and intercept parameters for E and ρ . Here we include our data for 8-mers: although these simulations do not adequately probe the glass formation range to report sufficiently on supercooled dynamics, they do provide good data on thermodynamic quantities. As shown by Figure 13a, 97% of the variation in E_m is predicted by a linear dependence on E_b ($R^2 = 0.97$). A similar relationship is seen between ρ_m and ρ_b , albeit with only 56% of the variation in ρ_m predicted by a linear dependence on ρ_b (Figure 13b, $R^2 = 0.56$). This apparent difference in the strength of these correlations is simply a result of the scaling of E with n that is absent for ρ . If we instead assess these correlations at fixed molecular size, R^2 drops to the vicinity of 0.5 in both cases (see SI). In any case, there is apparently at least a rough tendency for a stronger temperature dependence of the density or larger pairwise partial specific heat for these molecules to be accompanied by a lower extrapolated zero-temperature intercept of that

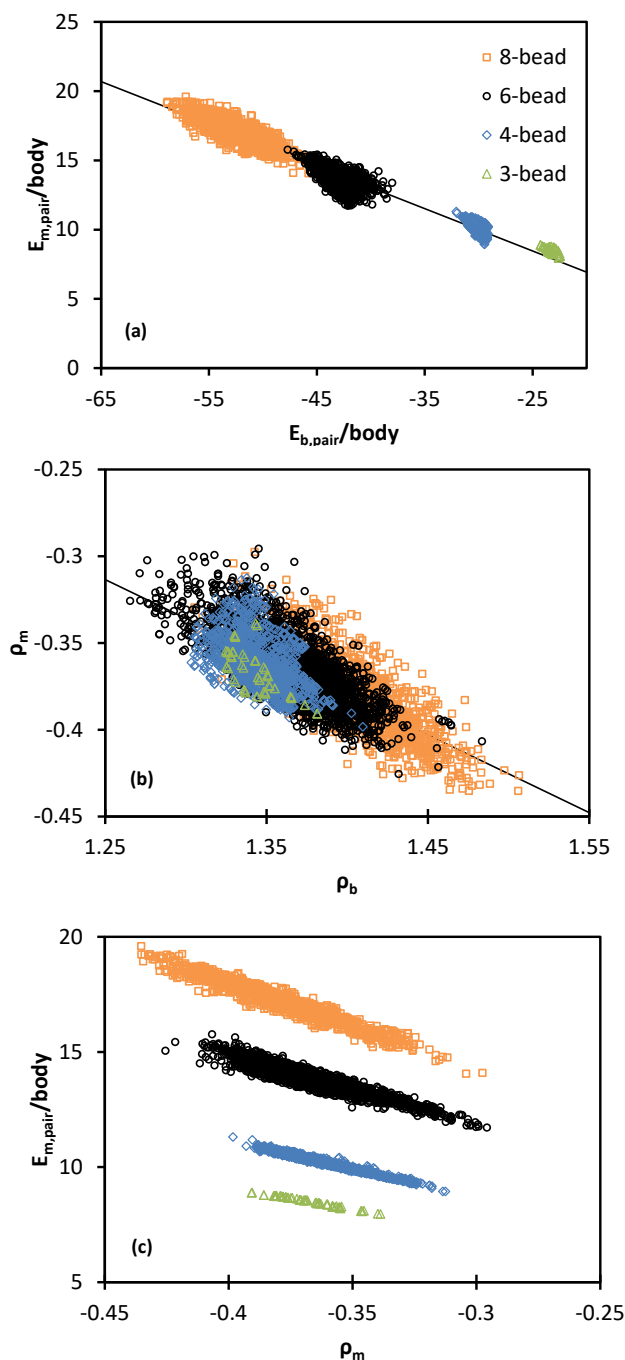


Figure 12. Temperature dependence vs 0 K extrapolated intercept parameter for the (a) pair energy and (b) density. (c) Temperature dependence of the pair energy vs that of the density. Data are for all 3-bead (green triangles), 4-bead, (blue diamonds), 6-bead (black circles), and 8-bead (orange squares) rigid molecules simulated by the genetic algorithm.

thermodynamic quantity. What are the implications of this finding?

This type of phenomenology is commonly referred to as entropy-enthalpy compensation. It is typically rationalized as resulting from a trade-off between entropy and enthalpy as some third property of the system is varied⁶⁷. Given that, for a chosen molecule size, we find that pair energy is closely correlated with density (Figure 13c), it would appear that both

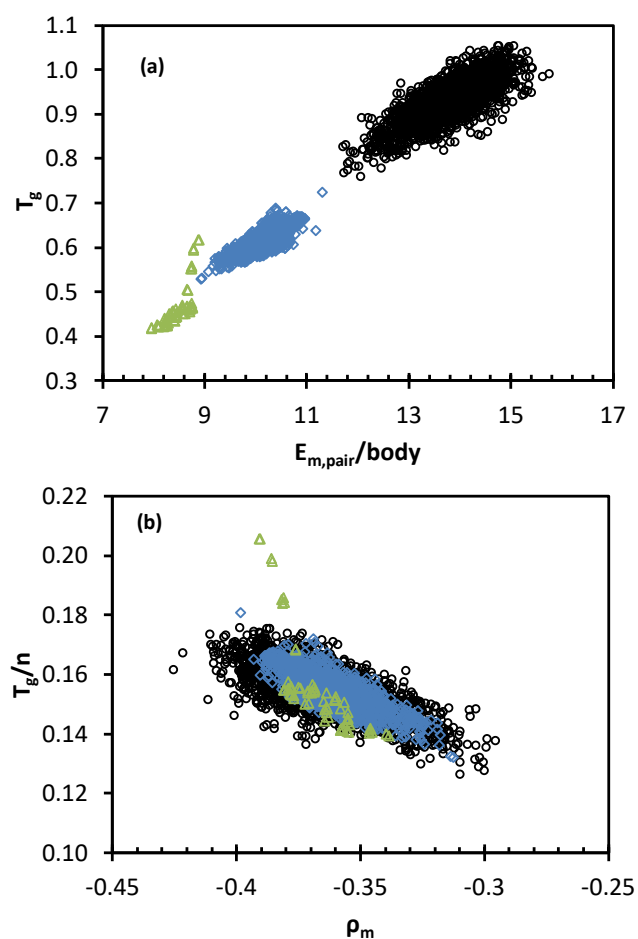


Figure 13. (a) T_g vs temperature-dependence of the pair energy per body and (b) T_g/n temperature dependence of the density, for all 3-bead (green triangles), 4-bead, (blue diamonds), and 6-bead (black circles) rigid molecules simulated by the genetic algorithm.

the density and pair energy fundamentally reflect variations in molecular packing in these systems. The entropy-enthalpy compensation effect thus implies that molecules with more favourable enthalpic driving forces for tight molecular packings have less favourable entropic factors associated with tight molecular packing. These molecules thus have higher extrapolated zero-temperature densities and lower extrapolated zero-temperature activation energies, but with a tendency for these improved packings to be lost at higher temperatures where entropy dominates.

A central feature any entropy-enthalpy compensation effects is the presence of a 'compensation temperature' at which the enthalpic and entropic contributions compensate, such that all systems obeying the compensation law exhibit the same behaviour. This temperature is given by the negative inverse of the slope of the linear relations observed in Figure 13 and is found to be $T_{comp} \cong 3.3$ for the pair energy and $T_{comp} \cong 2.2$ for the density. Since these compensation temperature are much higher than the onset temperature of glass formation for all of these systems, this implies that systems with higher E_m and lower E_b will have a lower (more favourable) pair energy over the entire temperature range relevant to glass formation, while systems with a higher ρ_m (note that ρ_m is negative, such that this

implies a lower thermal expansion coefficient) and lower ρ_b will have a lower density over the entire relevant temperature range.

We now turn to the question of how T_g and m relate to these underlying thermodynamic quantities. As shown by Figure 13, T_g correlates well with both E_m and ρ_m . The fraction of variation in T_g within each molecule size accounted for by each of these correlations ranges from 0.50 to 0.77 depending on molecular size. In contrast, as shown by Figure 14a and b, fragility does not exhibit appreciable correlations with either quantity ($R^2 < 0.15$ in all cases at a single-molecule-size level).

The question of whether fragility exhibits any correlation with density is salient to the underlying nature of glass formation. Prior work has shown that the Adam-Gibbs entropy theory of glass formation leads to a scenario wherein fragility is correlated with increased packing frustration⁸, which can be associated with reduced dimensionless density or enhanced thermal expansion coefficient. The thermal expansion coefficient α can be written in terms of our density fit parameters as

$$\alpha = -\frac{1}{T + \frac{\rho_b}{\rho_m}} \quad (8)$$

Any correlation of m with α would thus require a correlation of with the ratio $-\rho_b/\rho_m$. As shown by Figure 14c, no such correlation is present in these data. While density is certainly a coarse measure of molecular packing, these results call into question whether “packing frustration” concepts emerging from proposed thermodynamic theories of the glass transition provide a useful predictor of glass-formation behaviour.

Discussion and Conclusions

In summary, these results provide new insights into the relationship between molecular structure and glass formation behaviour. They indicate that the fragility of these rigid model molecules is primarily controlled by molecular anisotropy. Specifically, near-extended non-crystallizing shapes tend to have low fragility, while compact shapes tend to have high fragility. We also find a narrow regime of highly extended molecules tending to have both high T_g and high fragility and to exhibit increases in both quantities with increasing degrees of extendedness. This regime is quickly lost with increasing size of these rigid molecules, likely due to crystallization in long rigid rods.

Outside of this regime, the glass transition temperature is not predicted by molecular anisotropy. Instead, it is in general most strongly predicted (among the quantities we tested) by packing-related quantities such as density and pair energy. We note that this finding *should not* be taken to indicate that T_g is controlled by any universal relationship with density, but only that this is a leading controller of T_g in the case of fixed homogenous interactions in stiff molecules. These findings also demonstrate that the glass transition temperature and the fragility of glass

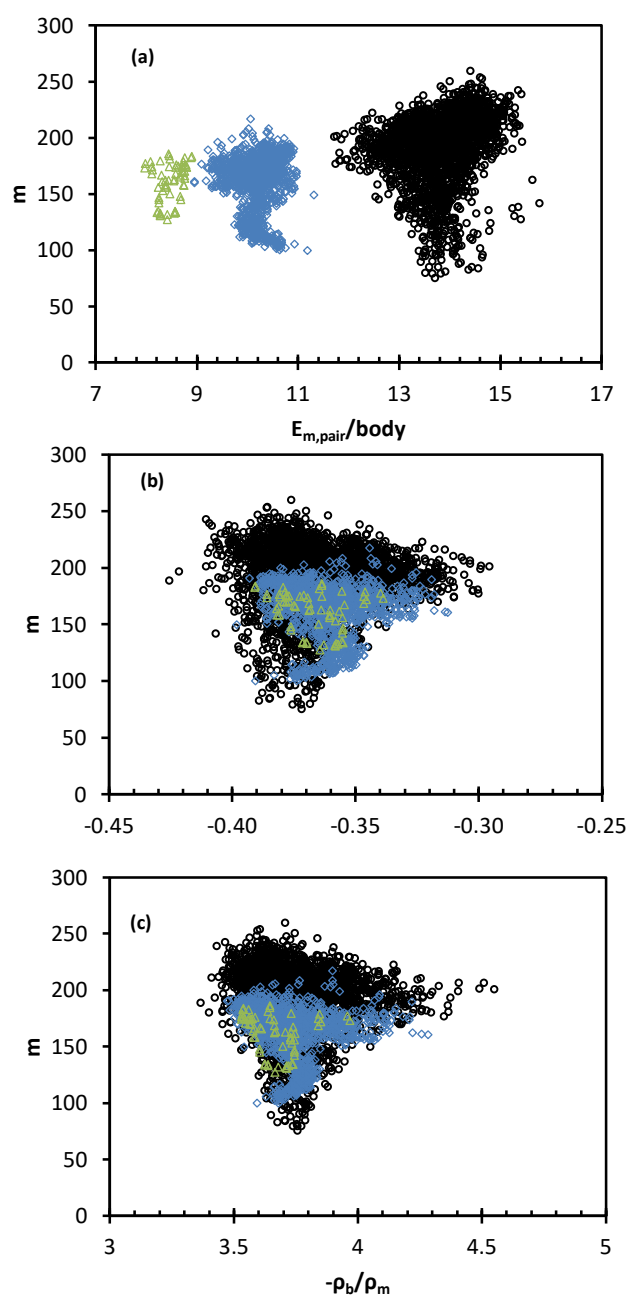


Figure 14. Kinetic fragility index vs (a) temperature dependence of the pair energy, (b) temperature dependence of the density, and (c) ratio of 0 K extrapolated intercept parameter to temperature dependence of the density, for all 3-bead (green triangles), 4-bead, (blue diamonds), and 6-bead (black circles) rigid molecules simulated by the genetic algorithm.

formation do not exhibit any universal correlation and can be decoupled by simultaneously varying molecular size and anisotropy. This has considerable potential practical implications. For example, applications rubbery engineering polymers dynamic load applications require a low T_g ; independent control of the fragility (and thus of the temperature dependence of the viscosity or loss modulus) would permit rational control of dissipative contributions to the mechanical response that play a key role in performance under dynamic mechanical load.

We note that while these conclusions have been illustrated based upon values of the glass transition temperature and kinetic fragility index that have been extrapolated to an experimental timescale, use of these values as defined based on a directly-accessed computational timescale does not qualitatively alter our findings. Illustrative data to this effect can be found in the supplementary material.

For small molecules and molecules exhibiting high stiffness due to (for example) high levels of conjugation, these findings may provide direct insight into the relationship between fragility and molecular shape at fixed interaction strength. For larger and more flexible molecules such as polymers, it is common to decompose dynamics into motions of near-rigid rigid sub-units (such as the Kuhn segment in polymer theory). For these molecules, we would expect the insights identified here to apply at the level of this basic quasi-rigid dynamical unit. As noted above, these polymeric dynamical subunits are in many cases relatively extended due to polymer backbone stiffness, and they may thus frequently correspond to the extremely-extended limit observed here where both T_g and fragility are observed to increase with molecular extendness. If so, these results might rationalize the common tendency for increasing polymer stiffness to correlate with increases in T_g and fragility⁶. This finding may also be related to arguments to the effect that the molecular weight dependence of T_g in polymers may be driven by the molecular-weight dependence of the size of the dynamical subunit rather than by explicit chain end effects⁶⁴. An extension of the present findings to polymers comprised of chains of these rigid molecules could provide additional insight in this direction.

Beyond the structure/property relations, these results have implications for the fundamental understanding of the glass transition. A large number of theoretical frameworks have been proposed to describe the underlying physics of the glass transition. The inability to determine which of these theoretical frameworks is correct represents a central challenge in the field. One of the natural questions regarding any theory of glass formation is whether it can predict and rationalize the range of fragilities seen in experiment; the present data provide a useful test set for asking this question. For example, we do not find that fragility is correlated with 'packing-related' thermodynamic quantities including the density, thermal expansion coefficient, or pair energy. This finding is evidently problematic for theoretical frameworks⁸ that predict a link between fragility and 'packing frustration'. On the other hand, at this time we cannot assess the validity of theoretical predictions connecting fragility to the change in the specific heat across the glass transition⁶⁸, since our quench algorithm does not access the glassy state.

Explicit predictions for the relationship between molecular shape and dynamics in the glass formation range have been made by Tripathy and Schweizer based on both the mode-coupling theory and the Nonlinear Langevin Equation theory of liquid dynamics, both for hard model molecules^{19,20} and attractive model molecules directly comparable to those

simulated here^{21,22}. The latter theory, while conceptually retaining the force-based approach to dynamics of the mode-coupling theory, admits activated relaxation and is therefore more directly relevant to our findings. Tripathy and Schweizer reported predictions for the dynamic fragility of athermal rigid molecules composed of multiple sites as a function of their geometry¹⁹. Their predictions (see figure 7 in that paper) suggest the following ranking of fragilities of glass formation from low to high:

10-site rod < 6-site rod \cong hexagon < 2-site rod \cong 8-site disk \cong 5-site disk \cong triangle \cong sphere < cube \cong tetrahedron < octahedron \cong snub disphenoid \cong gyroelongated square pyramid.

Not all of these specific shapes were simulated as part of our study. However, this ranking appears to be in good accord with our findings. Our results specifically confirm the prediction that highly extended shapes of increasing length represent the lower-limit of fragilities within the family of rigid multi-site molecules. In the other limit, both our simulations and the NLE theory predict that the most fragile geometries are quite compact. Additionally, the theory's predictions are in *quantitative* agreement with our simulations with respect to the *range* of fragilities accessible by tuning shape in these molecules: the NLE theory predicts a factor of 3 variation in fragility from the least to most fragile glass-formers in this class; our Figure 8a reports m ranging from 84 to 260 at the extrapolated 100-second timescale, which is almost exactly a factor of 3 range.

Within the NLE theory, dynamics occur through locally activated hopping of particles escaping local cages. Increases in fragility reflect, within this framework, differences in the temperature dependence of the local caging behaviour of the fluid, which is ultimately related to the pair correlation function. Critically, the caging scale is not related in a simple way to density, rationalizing the lack of clear correlations of this kind in our data.

Beyond these immediate findings, these results establish a new set of valuable minimal computational models enabling study of glass formation in systems spanning a wide range of fragilities of glass formation. Angular specifications for construction of these extremal molecules, shown in Figure 8, via the algorithm described in the methods section are provided in the SI. Prior work has pointed to a critical need to probe extremes of fragility in the effort to understand the glass transition³, and these models provide a minimal computationally efficient strategy to this end.

Finally, this work provides a pilot validation of simulation-based evolutionary design of model glass-forming molecules with targeted fragilities of glass formation. In the long term, this approach should be extensible to evolutionary design of glass formation in chemically-realistic molecules.

Conflicts of interest

There are no conflicts to declare.

Acknowledgements

The authors acknowledge K. Schweizer for valuable discussions. This work was supported by a generous grant from the W. M. Keck Foundation. This material is based in part on work supported by the National Science Foundation NSF Career Award grant number DMR1554920.

Notes and References

- 1 P. G. Debenedetti and F. H. Stillinger, *Nature*, 2001, **410**, 259–267.
- 2 A. Cavagna, *Phys. Rep.-Rev. Sect. Phys. Lett.*, 2009, **476**, 51–124.
- 3 S. A. Kivelson and G. Tarjus, *Nat. Mater.*, 2008, **7**, 831.
- 4 S. Sastry, *Nature*, 2001, **409**, 164–167.
- 5 C. A. Angell, *J. Phys. Chem. Solids*, 1988, **49**, 863–871.
- 6 A. P. Sokolov, V. N. Novikov and Y. Ding, *J. Phys. Condens. Matter*, 2007, **19**, 205116.
- 7 K. Kunal, C. G. Robertson, S. Pawlus, S. F. Hahn and A. P. Sokolov, *Macromolecules*, 2008, **41**, 7232–7238.
- 8 J. Dudowicz, K. F. Freed and J. F. Douglas, in *Advances in Chemical Physics*, Wiley, 2008, vol. 137, pp. 125–222.
- 9 M. L. Hoarfrost and R. A. Segalman, *Macromolecules*, 2011, **44**, 5281–5288.
- 10 M. L. Hoarfrost and R. A. Segalman, *ACS Macro Lett.*, 2012, **1**, 937–943.
- 11 U. H. Choi, A. Mittal, T. L. Price Jr., M. Lee, H. W. Gibson, J. Runt and R. H. Colby, *Electrochimica Acta*, 2015, **175**, 55–61.
- 12 M. T. Cicerone and J. F. Douglas, *Soft Matter*, 2012, **8**, 2983–2991.
- 13 M. T. Cicerone and C. L. Soles, *Biophys. J.*, 2004, **86**, 3836–3845.
- 14 C. A. Angell, *Science*, 1995, **267**, 1924–1935.
- 15 D. Huang and G. B. McKenna, *J. Chem. Phys.*, 2001, **114**, 5621.
- 16 V. N. Novikov and A. P. Sokolov, *Nature*, 2004, **431**, 961–963.
- 17 K. Niss, C. Dalle-Ferrier, G. Tarjus and C. Alba-Simionesco, *J. Phys. Condens. Matter*, 2007, **19**, 076102.
- 18 T. K. Patra, V. Meenakshisundaram, J.-H. Hung and D. S. Simmons, *ACS Comb. Sci.*, 2017, **19**, 96–107.
- 19 M. Tripathy and K. S. Schweizer, *J. Chem. Phys.*, 2009, **130**, 244907.
- 20 M. Tripathy and K. S. Schweizer, *J. Chem. Phys.*, 2009, **130**, 244906.
- 21 M. Tripathy and K. S. Schweizer, *Phys. Rev. E*, 2011, **83**, 041406.
- 22 M. Tripathy and K. S. Schweizer, *Phys. Rev. E*, 2011, **83**, 041407.
- 23 K. S. Schweizer and E. J. Saltzman, *J. Chem. Phys.*, 2003, **119**, 1181.
- 24 M. Z. Miskin and H. M. Jaeger, *Nat. Mater.*, 2013, **12**, nmat3543.
- 25 A. D. Griffith and R. S. Hoy, *Phys. Rev. E*, , DOI:10.1103/PhysRevE.98.042910.
- 26 A. D. Griffith and R. S. Hoy, *ArXiv190700035 Cond-Mat*.
- 27 E. D. Salcedo, H. T. Nguyen and R. S. Hoy, *ArXiv190709616 Cond-Mat*.
- 28 W. Kob and H. C. Andersen, *Phys. Rev. Lett.*, 1994, **73**, 1376–1379.
- 29 S. Sastry, P. G. Debenedetti and F. H. Stillinger, *Nature*, 1998, **393**, 554–557.
- 30 F. Sciortino, W. Kob and P. Tartaglia, *Phys. Rev. Lett.*, 1999, **83**, 3214–3217.
- 31 B. Coluzzi, G. Parisi and P. Verrocchio, *J. Chem. Phys.*, 2000, **112**, 2933–2944.
- 32 S. Plimpton, *J. Comput. Phys.*, 1995, **117**, 1–19.
- 33 H. Kamberaj, R. J. Low and M. P. Neal, *J. Chem. Phys.*, 2005, **122**, 224114.
- 34 M. E. Tuckerman, G. J. Martyna and B. J. Berne, *J. Chem. Phys.*, 1990, **93**, 1287–1291.
- 35 J.-H. Hung, T. K. Patra, V. Meenakshisundaram, J. H. Mangalara and D. S. Simmons, *Soft Matter*, 2019, **15**, 1223–1242.
- 36 L. Martínez, R. Andrade, E. G. Birgin and J. M. Martínez, *J. Comput. Chem.*, 2009, **30**, 2157–2164.
- 37 R. J. Lang, W. L. Merling and D. S. Simmons, *ACS Macro Lett.*, 2014, **3**, 758–762.
- 38 D. Ruan and D. S. Simmons, *Macromolecules*, 2015, **48**, 2313–2323.
- 39 D. Ruan and D. S. Simmons, *J. Polym. Sci. Part B Polym. Phys.*, 2015, **53**, 1458–1469.
- 40 R. J. Lang and D. S. Simmons, *Macromolecules*, 2013, **46**, 9818–9825.
- 41 R. A. Riggleman, K. Yoshimoto, J. F. Douglas and J. J. de Pablo, *Phys Rev Lett*, 2006, **97**, 0455021–0455024.
- 42 W. L. Merling, J. B. Mileski, J. F. Douglas and D. S. Simmons, *Macromolecules*, 2016, **49**, 7597–7604.

- 43 J. H. Mangalara, M. D. Marvin and D. S. Simmons, *J. Phys. Chem. B*, 2016, **120**, 4861–4865.
- 44 B. A. P. Betancourt, J. F. Douglas and F. W. Starr, *Soft Matter*, 2012, **9**, 241–254.
- 45 W. Zhang, J. F. Douglas and F. W. Starr, *J. Chem. Phys.*, 2017, **147**, 044901.
- 46 P. Z. Hanakata, J. F. Douglas and F. W. Starr, *Nat. Commun.*, 2014, **5**, 4163.
- 47 J. H. Mangalara, M. D. Marvin, N. R. Wiener, M. E. Mackura and D. S. Simmons, *J. Chem. Phys.*
- 48 J. H. Mangalara, M. E. Mackura, M. D. Marvin and D. S. Simmons, *J. Chem. Phys.*
- 49 A. Shavit and R. A. Riggleman, *Macromolecules*, , DOI:10.1021/ma400210w.
- 50 C. Bennemann, W. Paul, J. Baschnagel and K. Binder, *J. Phys. Condens. Matter*, 1999, **11**, 2179.
- 51 H. Vogel, *Phys Zeit*, 1921, **22**, 645–646.
- 52 G. S. Fulcher, *J. Am. Ceram. Soc.*, 1925, **8**, 339–355.
- 53 Tammann, G. and Hesse, W., *Z Anorg Allg Chem*, 1926, **156**, 245–257.
- 54 V. Meenakshisundaram, J.-H. Hung, T. K. Patra and D. S. Simmons, *Macromolecules*, , DOI:10.1021/acs.macromol.6b01747.
- 55 D. Turnbull and M. H. Cohen, *J. Chem. Phys.*, 1961, **34**, 120–125.
- 56 G. Adam and J. H. Gibbs, *J Chem Phys*, 1965, **43**, 139–146.
- 57 K. F. Freed and J. Dudowicz, *Macromolecules*, 1998, **31**, 6681–6690.
- 58 K. F. Freed and J. Dudowicz, *Macromol. Symp.*, 2000, **149**, 11–16.
- 59 Q. Qin and G. B. McKenna, *J. Non-Cryst. Solids*, 2006, **352**, 2977–2985.
- 60 V. Sharma, K. Park and M. Srinivasarao, *Mater. Sci. Eng. R Rep.*, 2009, **65**, 1–38.
- 61 P. G. Bolhuis, A. Stroobants, D. Frenkel and H. N. W. Lekkerkerker, *J. Chem. Phys.*, 1997, **107**, 1551–1564.
- 62 S. Mirigian and K. S. Schweizer, *J. Chem. Phys.*, 2014, **140**, 194506.
- 63 S. Mirigian and K. S. Schweizer, *J. Chem. Phys.*, 2014, **140**, 194507.
- 64 S. Mirigian and K. S. Schweizer, *Macromolecules*, 2015, **48**, 1901–1913.
- 65 W. Ping, D. Paraska, R. Baker, P. Harrowell and C. A. Angell, *J. Phys. Chem. B*, 2011, **115**, 4696–4702.
- 66 A. Simperler, A. Kornherr, R. Chopra, P. A. Bonnet, W. Jones, W. D. S. Motherwell and G. Zifferer, *J. Phys. Chem. B*, 2006, **110**, 19678–19684.
- 67 L. Liu and Q.-X. Guo, *Chem. Rev.*, 2001, **101**, 673–696.
- 68 V. Lubchenko and P. G. Wolynes, *Annu. Rev. Phys. Chem.*, 2007, **58**, 235–266.